

DRAFT VERSION MAY 1, 2025

Typeset using L^AT_EX **modern** style in AASTeX7

X-ray Spectroscopy via Temporal Decomposition

WILLIAM SETTERBERG ¹ AND LINDSAY GLESENER ¹¹ *University of Minnesota*

ABSTRACT

We present a novel way to fit solar flare X-ray spectra that offers more sensitivity to physical flare parameters than traditional approaches to spectroscopy. We decouple physically distinct emission types in solar flare X-ray spectra using timing behaviors, a technique we call time-decomposed spectroscopy. By fitting the shapes of particular time series to others across a time interval, we extract X-ray emission of distinct physical origins before any forward modeling. We perform spectroscopy on the original and time-decomposed spectra and find good agreement, with physical reasons for the few disagreements. In general, the time decomposition technique provides more precise results than those of traditional spectroscopy. The thermal and nonthermal energies are better constrained by more than an order of magnitude using the time decomposition approach, relative to traditional spectroscopy. We explain mathematically how and why the technique works using the multifractal formalism, and show that fractality is one way to choose appropriate light curves for this analysis. We speculate about applications to different wavelengths for solar data analysis, as well as applications to other physics subfields and domains.

1. INTRODUCTION

Solar flares energize particles to keV energies via heating and nonthermal mechanisms. Particles accelerated to energies much greater than the thermal energy (a.k.a. nonthermal particles) make up a significant fraction of the flare energy budget (R. P. Lin & H. S. Hudson 1976). Generally, nonthermal particles in solar flares follow a power law distribution in energy, so most of their energy is allocated to the lower-energy nonthermal particles. However, measuring the low-energy behavior of these nonthermal electron populations is difficult, and remains the largest contributor to the nonthermal energy uncertainty (P. Saint-Hilaire & A. O. Benz 2005). The transition from hot plasma X-ray emission (thermal bremsstrahlung) to e.g. cold, thick target power-law nonthermal emission (J. C. Brown 1971) occurs in an energy range which is dominated by thermal bremsstrahlung emission. In other words, it is hard to fit the low-energy cutoff parameter E_c assumed by the cold, thick target model using traditional spectroscopy. Current spectroscopy methods lead to degenerate solutions even with the simplest composite models, and without better tools to explore X-ray

data, we cannot confidently investigate more complex physics, such as the low-energy shape of nonthermal particle populations. Better understanding the low-energy behavior of the electron population would yield physical insights for observers, modelers, and experimentalists alike about solar flare physics.

Motivated by this, we present a new approach to spectroscopy. We exploit timing differences in thermal and nonthermal X-ray time profiles to aid in spectroscopy. Often, nonthermal X-ray fluctuations occur on timescales of a few seconds (P. C. Grigis & A. O. Benz 2004), and on shorter than one second in select cases (A. L. Kiplinger et al. 1983; J. Qiu et al. 2012; J. Cheng et al. 2013; T. Knuth & L. Glesener 2020). The nonthermal timing fluctuations are relatively fast because they are directly associated with electron acceleration and transport. In contrast, variations in thermal bremsstrahlung emission occur on timescales of minutes to tens of minutes, and sometimes appear as quasi-periodic pulsations (A. R. Inglis et al. 2015; L. A. Hayes et al. 2020). These timescales are longer because the plasma takes time to heat.

We use the differences in these timescales to sift emission per energy bin by temporal behavior. We describe this approach in precise equations, which are straightforward to apply. We apply this approach to two flares, Flare F1 observed by the Spectrometer/Telescope for Imaging X-rays (STIX, S. Krucker et al. (2020)), and Flare F2 observed by the Reuven Ramaty High-Energy Solar Spectroscopic Imager (RHESSI, R. P. Lin et al. (2002)). RHESSI uses time modulation to perform Fourier imaging, while STIX uses spatial modulation. In both cases, the decomposition produces physically reasonable results.

We compare energy computation results and show that the time-decomposition technique places more precise bounds on the nonthermal energy deposited, and slightly more precise bounds on the flare plasma thermal energy. We discuss the physics of how timing can lift some degeneracies intrinsic to traditional spectroscopy. We discuss potential applications to multiple wavelengths and the irrelevance of periodic behavior. Finally, we explain how the multifractal formalism may be used in tandem with the time decomposition technique.

2. TEMPORAL DECOMPOSITION OF X-RAY TIME SERIES

2.1. *An intuitive description*

The temporal decomposition method uses differences in timing characteristics between solar thermal and nonthermal X-ray bremsstrahlung to decompose spectra along the energy dimension. First, we illustrate the basic approach by means of example. Figure 1 shows X-ray light curves for Flare F1, observed on 2022 April 20 by STIX. The black light curve in the figure is dominated by emission from thermal plasma, while the blue light curve is dominated by nonthermal bremsstrahlung, which exhibits more abrupt changes associated with multiple energy release events during the flare. During the impulsive phase, the red curve is a mix of thermal and nonthermal bremsstrahlung, and exhibits some short- and some longer-timescale behavior.

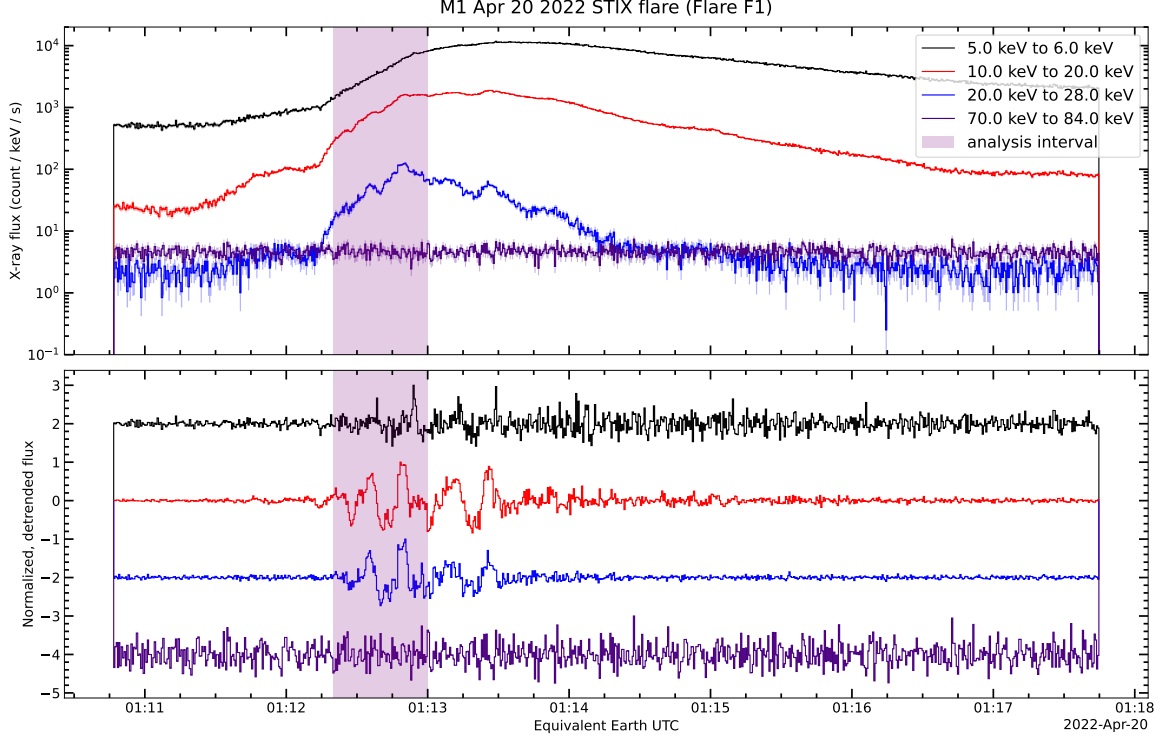


Figure 1. X-ray light curves for an M-class flare observed by Solar Orbiter/STIX; we call this **Flare F1**. The pink region is the analysis interval. Times are adjusted for 1 AU photon arrival time, so they are a few minutes later than the UTC times recorded aboard Solar Orbiter. The red and blue curves correspond to higher-energy X-rays, and the detrended plots show how these exhibit relatively more intense variations within the analysis interval than the lower energy (black) light curve does. The indigo curve is detector background, entirely comprised of uncorrelated shot noise. The detrended curves are high-pass filtered. The detrending was performed using a zero-lag fifth-order low-pass Butterworth filter with a cutoff frequency corresponding to 20s (S. Butterworth et al. 1930; F. Gustafsson 1996).

Traditionally, the emission over an analysis time interval would be integrated together and fit simultaneously with a set of spectral models to determine how much thermal and non-thermal emission is present. Here, we present a different approach.

The key idea is to combine light curves across time and apply those combination coefficients across energy. In the case of Figure 1: we combine the thermal and non-thermal (black and blue) light curves across time with some weights to reconstruct the shapes of other light curves (like the red one). The weights of the blue and black curves, per energy, yield projection coefficients. Then, we sum the light curves across the analysis time interval into a counts vs. energy spectrum, and multiply the resulting energy spectra by those same time projection coefficients; this leverages temporal behavior to separate energetic components of the emitting plasma populations. **The result is that we separate the thermal and non-thermal emission before doing any spectral fitting; an example is shown in Figure 2.**

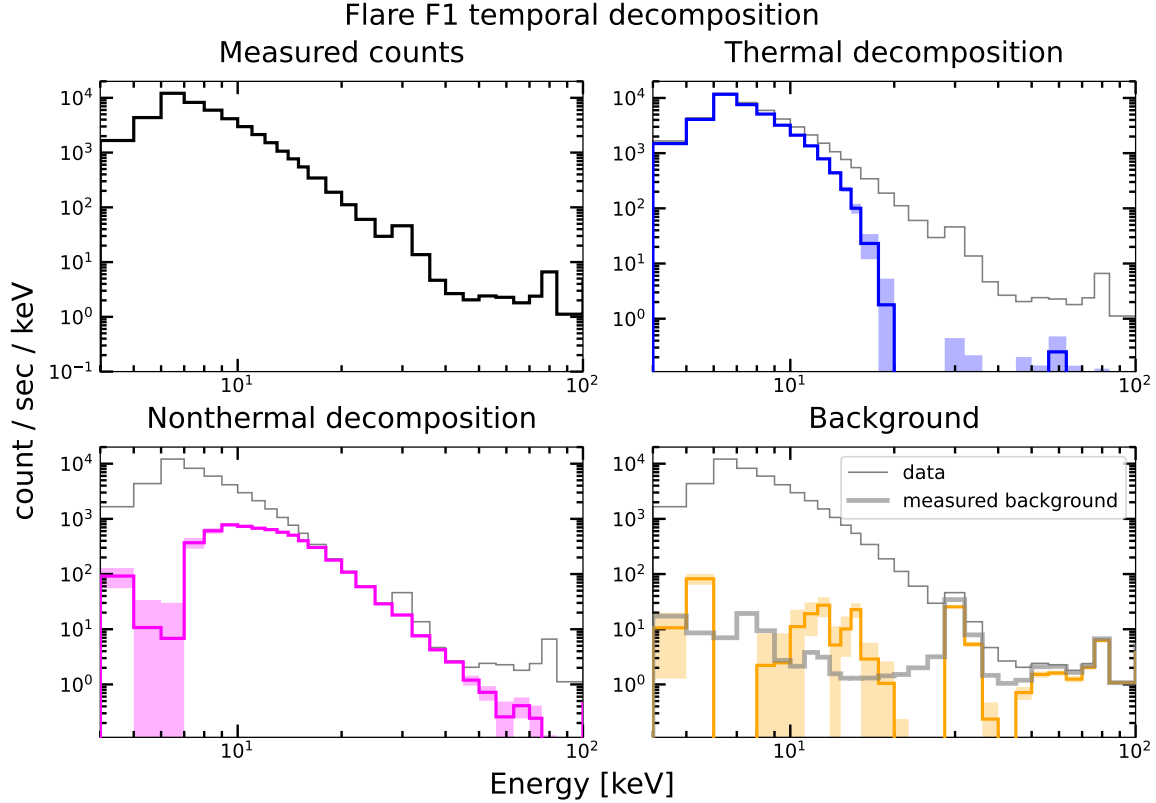


Figure 2. Time-decomposed spectra from Flare F1. The first panel shows the measured data; the second shows the time-decomposed thermal emission (blue); the third shows the time-decomposed nonthermal emission (magenta); the fourth panel shows the measured (gray) and time-decomposed (orange) backgrounds. Using only temporal variation to define the pseudobases in Equation 2, the spectra capture the background, thermal emission, and nonthermal emission with physically realistic spectral shapes, despite no spectroscopy yet being performed. In the fourth panel, a measured background from 19 April 2022 is overplotted on the decomposition. The decomposition technique captures the background well when its intensity is at least the order of that of the flare.

2.2. The decomposition formalism

We outline the formalism as follows. The relevant code is freely available online². First, we choose at least two pseudobasis vectors which are used to decompose the data across time—e.g. the black and blue light curves in Figure 1. The pseudobases should be as representative as possible of the different populations present in the data. In this case, we choose light curves we believe to be dominated by thermal and nonthermal emission, respectively. We call these light curves time pseudobases; the thermal pseudobasis is T and the nonthermal one is N .

Next, we normalize the light curves across time to address the intensity difference between lower- and higher-energy X-ray emission, which can be several orders of magnitude due to the steepness of solar flare X-ray spectra. We combine light curves along the energy axis to form an (E, t) spectrogram matrix with elements S_{ij} . The

² [GitHub: decomposition package](#); for paper-specific analysis questions, please contact the authors.

first index corresponds to energy and the second to time. In the case of STIX, the index $i \in \{0, 1, \dots, 29\}$ corresponds to its science energy bins, and $j \in \{0, 1, \dots, M\}$ the time bins across the purple interval in [Figure 1](#). For unnormalized data we use upper case letters, like S , N , T . For normalized spectrogram elements, we use lower-case letters, as in [Equation 1](#), where s_{ij} is a generic spectrogram element which has been normalized by total counts across a fixed time interval.

$$s_{ij} = \frac{S_{ij}}{\sum_k S_{ik}} \quad (1)$$

The values s_{ij} are unitless, so any type of data (e.g. flux, counts, count rate) may be used with this technique.

Next, we decompose all normalized light curves s_{ij} across time. The normalized nonthermal pseudobasis is n_j and thermal pseudobasis is t_j . The pseudobases do not have energy indices because they are implicitly associated with energy bins. We perform a multilinear regression across time as in [Equation 2](#). The constant offset term 1_j is normalized in the same way as N and T and written out explicitly to avoid confusion. The coefficient α_i is the portion of the arbitrary spectrogram element s_{ij} which behaves most like the thermal pseudobasis, β_i is that which is most like the nonthermal pseudobasis, and γ_i is a constant offset term which can account for the background if it is relatively constant across time. This technique can also account for time-varying backgrounds, which we describe later.

$$s_{ij} \approx \alpha_i t_j + \beta_i n_j + \gamma_i \frac{1_j}{\sum_k 1_k} \quad (2)$$

We estimate the pseudobasis vectors from the data using low- and high-energy light curves. Model predictions or external data sources may also form the pseudobases. If the element S_{ij} is not consistent to within a few percent, the technique is being applied inappropriately, and the pseudobases need to be reexamined.

After decomposing the spectra, we take the energy-dependent coefficients α_i β_i γ_i , and use them to project the temporal behavior of the time series across the energy axis of the spectrogram, as in [Equation 3](#).

$$S_{ij} \approx \left(\alpha_i \sum_k S_{ik} \right) \frac{T_j}{\sum_k T_k} + \left(\beta_i \sum_k S_{ik} \right) \frac{N_j}{\sum_k N_k} + \left(\gamma_i \sum_k S_{ik} \right) \frac{1_j}{\sum_k 1_k} \quad (3)$$

The colored/parenthesized portions of [Equation 3](#) are the time-decomposed energy spectra. Each normalized spectrogram element is explicitly written for notational consistency. The summation in the denominator of [Equation 1](#) has been multiplied to the right to form time-independent projections across energy of the various pseudobases.

We plot the colored coefficients from [Equation 3](#) as a function of energy for Flare F1 in [Figure 2](#). For all of the data in this work, we assume Gaussian statistics. The

errors are propagated via a Monte Carlo technique, wherein the original light curves are sampled using the count error distribution, and the resampled data is used to recompute the result many times. In [Figure 2](#), we observe that the blue and magenta curves have spectral shapes which closely match typical thermal and nonthermal emission spectra, and find that the background decomposition captures the “true” background when the emission is not source-dominated; the colors of the coefficients in [Equation 3](#) correspond to the colors of the plots. In [section 3](#), we show that the decomposed spectra represent physically meaningful components of the flare X-ray emission.

More generally, one may use any number of pseudobases in [Equation 2](#) and [Equation 3](#). In the case of RHESSI data, this is useful for fitting the background, as it varies with time. A high-energy light curve can be used as the background pseudobasis across time instead of a constant offset. A constant like the orange term in [Equation 3](#) may be added if desired or required, however a pseudobasis can often play the role of the background.

Furthermore, one may sum together one or more light curves to form a new pseudobasis, so long as the normalizations in [Equation 3](#) are respected. For the solar X-ray case, one may wish to sum a few thermal bremsstrahlung-dominated light curves and a few nonthermal bremsstrahlung-dominated light curves together to form energy-averaged thermal and nonthermal pseudobases.

After decomposing the spectra using timing information, we perform spectroscopy on the independent components. The temporal decomposition allows us to fit the thermal and nonthermal spectra separately, letting the models vary independently from one another, which reduces the degeneracy of spectral fits.

3. RESULTS

We apply time-decomposed spectroscopy to two GOES M-class solar flares. Flare F1—which has been examined some in prior sections—was observed by STIX on 20 April 2022 (M1 GOES class), and Flare F2 by RHESSI on 30 July 2011 (M9 GOES class). Both flares exhibit nonthermal emission in the $>\sim 25$ keV energies.

3.1. *Flare F1: 20 April 2022 flare observed by SolO/STIX*

First, we perform traditional and time-decomposed spectroscopy on Flare F1, from 2022-04-01T01:12:20Z to 01:13:00Z. The flare X-ray emission ([Figure 1](#)) is decomposed using the technique described in [section 2](#). The thermal pseudobasis is a sum of the three energy bins centered around 6 keV which capture the emission lines of highly-ionized iron present in the solar corona. The nonthermal one is a sum of three energy bins centered around 19 keV, where the nonthermal emission is dominant.

The counts and count errors are livetime-corrected, and errors are assumed to be normally distributed in all cases. We account for error on the counts due to Poisson statistics, as well as counts and livetime due to X-ray count and trigger count com-

Flare	Technique	Parameter	Best fit value	95% posterior interval
F1	traditional	T	23 MK	(16, 25) MK
F1	traditional	EM	$54 \times 10^{46} \text{ cm}^{-3}$	$(46, 160) \times 10^{46} \text{ cm}^{-3}$
F1	traditional	φ_e	$3.0 \times 10^{35} \text{ electron s}^{-1}$	$(1.9, 35) \times 10^{35} \text{ electron s}^{-1}$
F1	traditional	δ	6.5	(6.3, 6.8)
F1	traditional	E_c	21 keV	(14, 23) keV
F1	decomposition	T	20 MK	(20, 21) MK
F1	decomposition	EM	$88 \times 10^{46} \text{ cm}^{-3}$	$(77, 100) \times 10^{46} \text{ cm}^{-3}$
F1	decomposition	φ_e	$3.1 \times 10^{35} \text{ electron s}^{-1}$	$(2.8, 3.5) \times 10^{35} \text{ electron s}^{-1}$
F1	decomposition	δ	6.3	(6.1, 6.5)
F1	decomposition	E_c	22 keV	(21, 23) keV
F2	traditional	T	22 MK	(21, 23) MK
F2	traditional	EM	$2.1 \times 10^{49} \text{ cm}^{-3}$	$(1.6, 2.9) \times 10^{49} \text{ cm}^{-3}$
F2	traditional	φ_e	$5.7 \times 10^{35} \text{ electron s}^{-1}$	$(2.6, 390) \times 10^{35} \text{ electron s}^{-1}$
F2	traditional	δ	6.1	(5.9, 6.4)
F2	traditional	E_c	23 keV	(10, 27) keV
F2	decomposition	T	22 MK	(21, 23) MK
F2	decomposition	EM	$3.2 \times 10^{49} \text{ cm}^{-3}$	$(2.6, 3.9) \times 10^{49} \text{ cm}^{-3}$
F2	decomposition	φ_e	$1.2 \times 10^{35} \text{ electron s}^{-1}$	$(0.97, 1.7) \times 10^{35} \text{ electron s}^{-1}$
F2	decomposition	δ	5.2	(5, 5.3)
F2	decomposition	E_c	29 keV	(26, 32) keV

Table 1. The best-fit (minimized χ^2) parameters for flares F1 and F2, for both the traditional and time-decomposed fits. Errors and Markov chain Monte Carlo (MCMC) medians are also reported in the corner plots in [Appendix B](#).

pression, which STIX employs due to its small downlink volume ([S. Krucker et al. 2020](#)).

Before temporal decomposition, no systematic error is applied to the data. For both traditional and time decomposed spectroscopy, we apply a 20% systematic error to the smallest energy bin, and a 10% systematic error to all other energy bins. The systematic error is added in quadrature: $\sigma_{\text{tot}}^2 = \sigma_{\text{data}}^2 + (\sigma_{\text{sys}} \cdot \text{counts})^2$. The larger systematic uncertainty on the lowest energy bin reflects the relative complexity of characterizing the low-energy behavior of X-ray detectors—see, e.g., [S.-n. Ishikawa et al. \(2016\)](#)—as well as the evolving understanding of the STIX low-energy response.

After decomposition, we fit the blue curve (thermal decomposition) and magenta curve (nonthermal decomposition) in [Figure 2](#) completely independently. For the background pseudobasis, we sum three energy bins closest to 80 keV. We compare the background decomposition to the pre-flare background, and find that the background spectrum is well-modeled by the time decomposition when it is at least as intense as the flare emission.

We fit the livetime-adjusted counts using χ^2 minimization and run MCMC using the `emcee` Python package ([D. Foreman-Mackey et al. 2013](#)) on the χ^2 value to obtain parameter uncertainties; corner plots of the parameter posterior distributions are in [Appendix B](#). We also fit the X-ray spectra using typical X-ray spectroscopy where

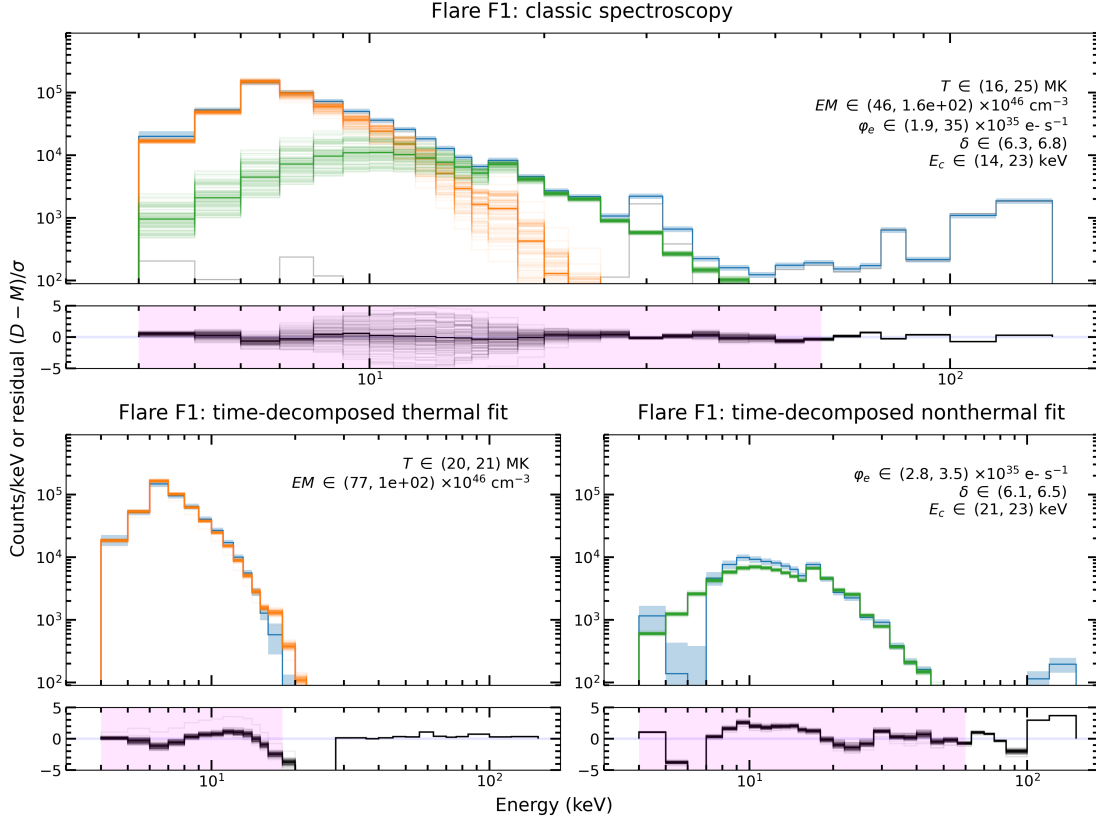


Figure 3. Comparison of traditional vs. time-decomposed spectroscopy for Flare F1 (M1 class 20 Apr 2022). The blue lines are the data, orange lines are the thermal bremsstrahlung fits, and green lines are the cold thick target fits. The pink regions in the residual plots indicate the energy fitting ranges. The top panel shows traditional spectroscopy and the bottom two panels show the results from the time-decomposed fits. The plots are annotated with 95% χ^2 parameter intervals. The spurious counts in the thermal decomposition at high energies are nonphysical and not included in the fit range.

both the thermal and nonthermal components are fit simultaneously, for comparison. The results for Flare F1 are displayed in Figure 3.

The model parameter intervals annotated on Figure 3 are the 95% χ^2 intervals for each spectroscopy method. All intervals overlap at the 95% level. Notably, however, the time-decomposed intervals are more precise than those of traditional spectroscopy. This better constrains the nonthermal electron power, as we discuss in section 4. The thermal bremsstrahlung function fit begins to diverge around ~ 18 keV, where the nonthermal flux is far brighter than the thermal flux. In the case of traditional spectroscopy, this energy would be totally dominated by nonthermal emission. We use this physical reasoning to restrict the fit range to ≤ 18 keV, and ignore spurious counts above this energy.

3.2. Flare F2: 30 July 2011 flare observed by RHESSI

We apply the same temporal decomposition technique to Flare F2, across a two-minute interval near the peak of the flare, after both RHESSI’s thick and thin attenuators have been inserted, from 2011-07-30T02:08:20Z to 2011-07-30T02:10:20Z.

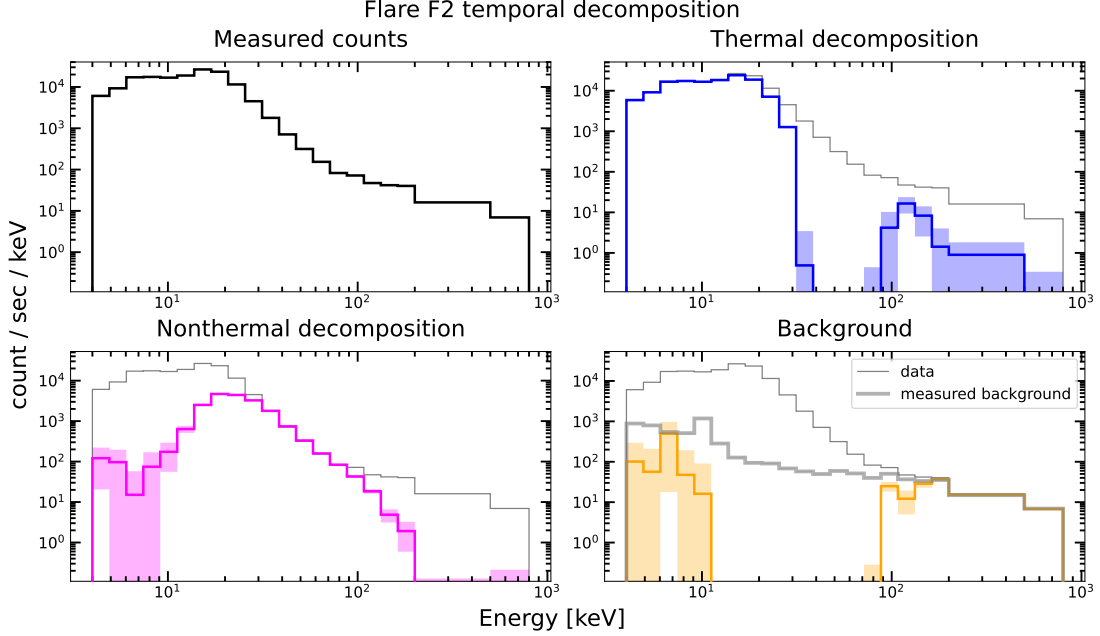


Figure 4. The data and time-decomposed components for Flare F2. The first panel shows the measured data; the second shows the time-decomposed thermal emission; the third shows the time-decomposed nonthermal emission; the fourth panel shows the measured and time-decomposed backgrounds. In the fourth panel, a pre-flare background is overplotted on the decomposition. As in the case of Flare F1, the decomposition technique captures the background well when its intensity is at least the order of that of the flare, despite the time-varying nature of RHESSI’s background.

We choose a sum of three bins near 6 keV as the thermal pseudobasis, the same for three bins near 80 keV for the nonthermal pseudobasis, and use a large energy band from 200 to 500 keV as the background pseudobasis. The decomposed spectra are presented in Figure 4.

A light curve of this flare in RHESSI, Fermi/GBM, and GOES XRS may be found in [T. Knuth & L. Glesener \(2020\)](#), Figure 1. Again we fit livetime-adjusted counts and use thermal bremsstrahlung and cold thick target models. Errors are assumed to be Gaussian and are taken from an `hsi_spectrum` IDL object output. No systematic uncertainty is added before the decomposition. Counts and errors are livetime corrected (divided by the livetime fraction). For both traditional and decomposed fitting, a uniform 10% systematic uncertainty is added in quadrature to the initial counts errors before spectroscopy. The temporally-decomposed and traditional spectroscopy results are displayed in Figure 5.

As is the case with STIX data, the temporal decomposition technique produces physically reasonable results. The systematic variation in the temporally decomposed χ^2 is more notable than in the traditional spectroscopy case. All parameters except the spectral index and electron flux overlap at the 95% χ^2 level.

There are a few notable distinctions between the fitting technique residuals. In the thermal model fits, the decomposed model underestimates the data $> \sim 20$ keV. This suggests a second, hotter source of X-rays may be present. We performed a fit with

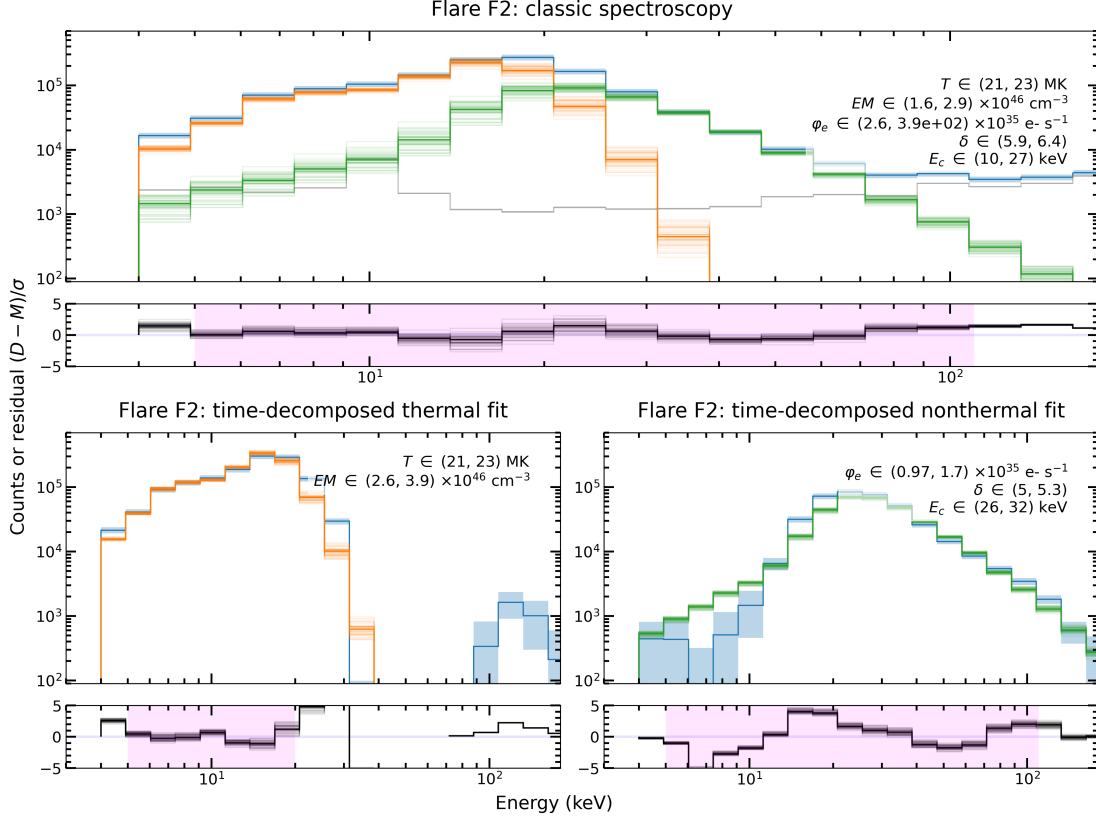


Figure 5. Comparison of traditional vs. time-decomposed spectroscopy for Flare F2 (M9 class 30 Jul 2011). The blue lines are the data, orange lines are the thermal bremsstrahlung fits, and green lines are the cold thick target fits. The pink regions in the residual plots indicate the energy fitting ranges. The gray line in the first panel is the background. The top panel shows traditional spectroscopy and the bottom two panels show the results from the time-decomposed fits. The plots are annotated with 95% χ^2 parameter intervals. There are many MCMC samples overplotted to give a sense of model variation. The spurious counts in the thermal decomposition at high energies are nonphysical and not included in the fit range; the corresponding high-energy residuals are small because of the very large error on these nonphysical counts.

a two-temperature model on the thermal time-decomposed spectrum; this assumes the thermal components vary similarly in time. We found good agreement up to 30 keV, with one component being about 18 MK and the other 30 MK (Figure 6), and this greatly improved the fit residuals. The emission measure of the superhot 30 MK component is an order of magnitude smaller than that of the 18 MK component.

Models with more free parameters generally fit data better. However, the hotter temperature we found is in agreement with prior studies of so-called superhot plasma, which is hypothesized to be the result of a small volume of low-density plasma being heated directly at the particle acceleration site in the corona (A. Caspi et al. 2014). The second temperature we find is in line with the statistics presented in A. Caspi et al. (2014), so this provides evidence that a second temperature component is likely present.

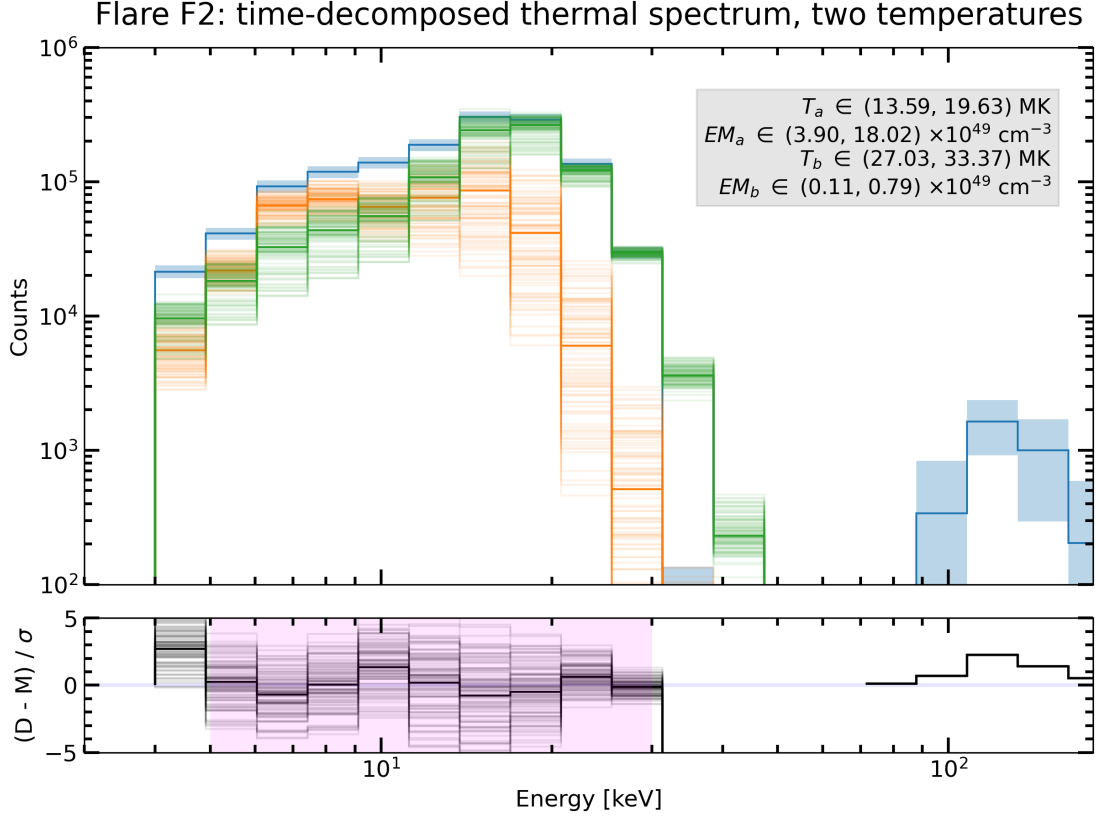


Figure 6. We fit two isothermal bremsstrahlung emission functions to the time-decomposed Flare F2 thermal spectrum. The time-decomposed data is blue; the high-energy portion is unphysical and ignored. We achieve better model/data agreement when fitting the two components: one is cool and high emission measure (orange), and the other is hot and lower emission measure (green).

In both spectroscopy approaches, there is a deficit in the high-energy ($> \sim 70$ keV) nonthermal component. This suggests a second electron population may be present in the form of a broken power law in electron space. The presence of such a break would be consistent with prior statistical studies of high-energy RHESSI flares (M. Alaoui et al. 2019). In contrast, there is disagreement around the low-energy shape of the nonthermal spectrum, as is also the case in Flare F1. This may be due to the presence of a different low-energy behavior between the two electron populations, or because the low-energy cutoff is not actually a sharp cutoff. It should be easier to see the true low-energy nonthermal shape in the time-decomposed case, as well as any ensuing disagreement between model and data. This idea is supported by the better constraint we place on the nonthermal parameters: in the traditional case, the electron flux spans two orders of magnitude, but is much better constrained in the time-decomposed fits.

Furthermore, traditional spectroscopy is very sensitive to background subtraction when the background intensity is comparable to the source intensity. The time decomposition technique inherently subtracts the background from the data, which pro-

vides better sensitivity in these regimes, and lets us follow the nonthermal behavior to higher and lower energies more confidently.

4. DISCUSSION

Here, we discuss the time-decomposition spectroscopy results in more detail. First, we quantify the energy content inferred from both spectroscopy techniques, and find they are consistent, but that the time-decomposition technique is much more precise. Next, we describe why using timing information lifts spectroscopy degeneracies, and go on to discuss intrinsic biases in both the traditional and time-decomposition techniques. Finally, we speculate about applications to cross-instrument analysis and entirely different types of data.

4.1. *Energetics*

Here we quantify the energy content of Flares F1 and F2, using results from traditional and time-decomposed spectroscopy. Because the time-decomposed technique leads to smaller 95% parameter intervals, the bounds on thermal and nonthermal energy are better than in the traditional case—sometimes significantly so.

We compute the volume of Flares F1 and F2 using geometry to estimate the thermal energy of the emitting plasma. While both flares were unocculted from the point of view of the respective HXR instrument, Flare F1 was partially occulted from the point of view of SDO/AIA. Because of this, we use slightly different approaches to compute the flare volumes. For Flare F1, we take the volume $V = h^3$ where h is the loop height. We use a geometric approach and knowledge of the flare center from the STIX perspective to estimate the height of the flare using SDO/AIA images. Taking into account a 4° occultation and the visible height in an SDO/AIA image, we estimate a height $h \approx 13$ Mm, and a flare volume $V \approx 2200 \text{ Mm}^3 = 2.2 \times 10^{27} \text{ cm}^3$. We estimate the thermal energy as $E_{\text{th}} \approx 2 \cdot \frac{3}{2} \sqrt{\text{EM} \cdot fV} k_B T$, where k_B is the Boltzmann constant, T is the isothermal plasma temperature, EM is the emission measure, and $f = 1$ is the geometric fill factor.

Flare F2 (M9 GOES class) was located on-disk from the Earth perspective. We approximate the most prominent flare loop as a semicircle and, using data from an AIA 94 Å image near the extreme ultraviolet peak, estimate the volume of the loop as a bent cylinder, finding $V \approx 18000 \text{ Mm}^3 = 1.8 \times 10^{28} \text{ cm}^3$.

Next we compute the nonthermal power and its time integral. Both flares appeared on-disk from the X-ray instrument perspectives, so we assume a cold, thick target model in both cases. Our assumed nonthermal electron distribution function is $f(E) = f_0 (E/E_0)^{-\delta}$, defined for $E \in [E_{\text{lo}}, E_{\text{hi}}]$, where $E_0 = 1$ keV is the nondimensionalization energy, f_0 is the normalization constant, and δ is the electron power law index. If we take the high-energy cutoff $E_{\text{hi}} \rightarrow \infty$, the deposited nonthermal energy across analysis interval Δt is $E_{\text{nth}} = \frac{1-\delta}{2-\delta} \varphi_e E_c \cdot \Delta t$, where φ_e is the electron flux and E_c the low-energy cutoff from spectroscopy.

Flare + emission	Which technique	Median energy (10^{30} erg)	95% χ^2 interval (10^{30} erg)
F1 thermal	traditional	0.50	[0.31, 0.88]
F1 thermal	decomposition	0.52	[0.48, 0.58]
F1 nonthermal	traditional	1.0	[0.35, 3.8]
F1 nonthermal	decomposition	0.54	[0.49, 0.59]
F2 thermal	traditional	5.7	[4.6, 7.0]
F2 thermal	decomposition	7.0	[6.0, 8.0]
F2 nonthermal	traditional	7.3	[1.7, 97]
F2 nonthermal	decomposition	0.94	[0.77, 1.2]

Table 2. The thermal energy is the average plasma energy estimate, while the nonthermal energy is the amount of energy deposited assuming a thick target scenario. In this table, we present the median energy value computed from 6000 MCMC samples for two reasons. First: the traditional spectroscopy methods have parameter posterior distributions with large skew. Second: the time-decomposition values are unimodal, so the difference between the best-fit and median values is negligible.

We compute the thermal and nonthermal energies for both spectroscopy techniques for the Flares F1 and F2, and tabulate the results in Table 2. The 95% intervals in Table 2 for the decomposition technique are smaller than the traditional intervals in all cases. **Our technique better constrains the Flare F1 nonthermal energy by an order of magnitude, and the Flare F2 nonthermal energy by two orders of magnitude.**

The most notable difference between techniques is the RHESSI nonthermal energy deposited. The spectroscopy interval occurs while both RHESSI attenuators are inserted. The attenuators block low-energy photons from both thermal and nonthermal distributions, which makes it even more difficult to constrain the low-energy nonthermal behavior. The decomposition technique may not suffer from this limitation as, even with reduced statistics, the nonthermal X-ray timing remains distinct from the thermal X-ray timing. However, as seen in Figure 5, the nonthermal decomposition has an interesting morphology around 10–20 keV, perhaps because the low-energy behavior of the nonthermal electron distribution is poorly modeled.

4.2. Timing information lifts degeneracies

Correlations between forward-fitted model parameters make it difficult to constrain physical properties of the emitting plasma. The time-decomposed spectroscopy technique lifts some of these degeneracies and gives better estimates of physical parameters of the electrons participating in the solar flare.

Isothermal bremsstrahlung and cold thick-target bremsstrahlung exhibit several correlations, exhibited in Figure 14 (Appendix B). In the case of isothermal bremsstrahlung emission, the temperature is strongly negatively correlated with the emission measure, a common occurrence in solar flare spectroscopy. There is competition between overall “brightness” of the flare (emission measure), along with the energetic spread of the assumed Maxwellian electron population which is emitting

X-rays (temperature). In the case of the cold target nonthermal bremsstrahlung, the cutoff energy E_c and the electron flux φ_e are also strongly negatively correlated: both contribute to the total number of electrons which hit the cold target.

When both models are fit simultaneously, other correlations emerge. By inspection of [Figure 14](#), we see that the electron spectral index δ is weakly correlated with temperature and emission measure. Furthermore, the cutoff energy and electron flux are not well-constrained. The same correlations and poor constraints are present in the corner plots for Flare F1, [Figure 11](#).

Contrast the simultaneous (thermal + nonthermal) fit results with time-decomposed spectroscopy, illustrated in [Figure 15](#) and [Figure 16](#). The shapes of the posterior distributions of parameters in the time decomposed case are unimodal and more normally distributed. The discrepancies between the data and the model found using the time-decomposition method indicate the places where our traditional physical models fail. As described in [subsection 3.2](#), performing a two-temperature fit on the decomposed data does lead to physically meaningful results, like the possible presence of superhot plasma. The enhancement in the nonthermal decomposition flux relative to the fitted model at low energies may also indicate the presence of additional structure in the nonthermal electron population.

4.3. *Intrinsic biases and limitations*

In applying this time-decomposed spectroscopy method, we make several simplifying assumptions—for example, that the plasma is isothermal, that the cutoff energy is sharp, and that there is only one power law of non thermal electrons with a single spectral index. However, all of these assumptions are also present in the traditional method of flare X-ray spectroscopy. The difference is that our method has better sensitivity to cases where those simple assumptions fail, such as in the isothermal assumption for Flare F2. [Figure 3](#) shows how uncertain the traditional spectroscopy fit is at fitting the low-energy portion of the thick target model. This will influence the possible values of cutoff energy and electron flux, and $E_{\text{nth}} \propto \varphi_e E_C$ —note, this convention is distinct from [G. D. Holman et al. \(2011\)](#), as their normalization cancels out a factor of the cutoff energy. Furthermore, the nonthermal spectral index may be influenced by the low-error bins of counts in the thermal/nonthermal transition regions, even though the collection of higher-energy count bins should dominate the cold target fitting. This has the effect of softening the photon spectrum, relative to the decomposition technique; this is reflected in the χ^2 intervals annotated in [Figure 3](#) and [Figure 5](#). The spectrum may appear softer because traditional spectroscopy performs a kind of averaging over the analysis interval, while the time-decomposition technique extracts the behavior of impulsive acceleration events more accurately.

Furthermore, it would be difficult to apply the “thick, warm” target model ([E. P. Kontar et al. 2015](#); [A. G. Emslie 2003](#)) to analyze time-decomposed data. The energy and pitch angle diffusion in the thick+warm target model is perhaps more physically

insightful than the traditional cold target assumption, and goes against the “thermal” vs “nonthermal” philosophy employed in the decomposition technique. However, one may still compare physical parameters obtained from the thick/warm target model with those from the temporal decomposition technique.

4.4. *Cross-instrument analysis*

Because the temporal decomposition technique uses only timing information for the mathematical operations, we may combine information from different instruments—and even vastly different wavelengths—using this technique. The temporal decomposition technique nondimensionalizes data during the fitting process, as noted immediately after Equation 1. For the flares analyzed here, one could construct a Fermi/GBM spectrogram from time-tagged event data with very fine time bins and combine it with STIX or RHESSI data to perform a dual-instrument simultaneous fit.

Traditionally, simultaneous fitting is achieved by maximizing a joint objective function. In the simultaneous temporal-decomposition case, simultaneous fitting would be achieved by first decomposing spectra in time and then maximizing one or more independent objective functions. Various wavelengths such as microwave and radio data could be combined to form temporal pseudobases; for example, type III radio burst data from PSP/FIELDS (S. D. Bale et al. 2016) could be used as part of a nonthermal basis, so long as the bursts are associated with prompt electron emission (S. Krucker et al. 2007). Microwave intensity curves from the Expanded Owens Valley Solar Array (EOVSA) could also be used as nonthermal bases. Light curves extracted from SDO/AIA images could be used as a pseudobasis for the slowly-varying thermal component of the flare. Such analyses would permit computations of the energy content of escaping electron beams associated with type III radio bursts, or investigating the properties of sunward vs. anti-sunward particle acceleration, as the anti-sunward accelerated particles lead to type III bursts. The gyrosynchrotron emission measured by EOVSAs is generally associated with higher-energy particles than those which produce bremsstrahlung X-rays, so if EOVSAs intensity profiles can be used as nonthermal pseudo bases, this would support the hypothesis that lower- and higher-energy particles are accelerated in the same way, which could provide some clarity for traditional joint X-ray and microwave fitting as in e.g. B. Chen et al. (2021).

5. WHY THIS WORKS: THE MULTIFRACTAL FORMALISM

The temporal decomposition works because of differences in temporal behaviors between thermal plasma and accelerated electrons. Here, we quantify the differences using the multifractal formalism, which is briefly described here, and defined more formally in Appendix A. We use the multifractal formalism to compute a distribution of time series sharpness, and use the sharpness distribution to discern different physical emission mechanisms, taking heavy inspiration from R. T. J. McAteer et al.

(2007) who performed similar analysis. Plots of function sharpness versus energy are constructed and explored intuitively in the context of thermal and nonthermal emission in solar flares.

Fractal systems are commonly found in nature and can often be described by a single fractal dimension D which describes how much space an object fills—or how rough an object is. A line is one dimension; self-similar shapes like the Sierpiński triangle fill more than one dimension, but not quite two dimensions. In contrast to these simpler systems, solar flare X-ray time series, solar wind turbulent dynamics, DNA sequences, and the stock market (R. T. J. McAtter et al. 2007; L. F. Gomes et al. 2023; J. P. Correia 2024; S. Drożdż et al. 2018) all exhibit behavior at multiple fractional dimension scales, and are therefore dubbed “multifractal” systems. We may quantify the presence of each fractal scale via a multifractal spectrum.

Intuitively, a multifractal spectrum describes the distribution of function sharpnesses across a given time series. The sharpness is quantified by a local scaling exponent called the Hölder exponent h .

Consider the two time series (left) and resulting multifractal spectra (right) in Figure 7. The green time series stays closer to the x axis and varies very quickly across time, like white noise; this is called antipersistent behavior and can be identified as a peak in the multifractal spectrum at $h < 0.5$. The blue time series is more smoothly varying and strays further from the mean; this is called persistent behavior and corresponds to $h > 0.5$. Prior work on this topic in the solar context has shown that thermal emission is generally more persistent, and nonthermal emission is more antipersistent (R. T. J. McAtter et al. 2007; R. T. J. McAtter & D. S. Bloomfield 2013). Thermal emission grows and decays slowly compared to the measurement cadence as plasma heats and cools, while nonthermal emission fluctuates quickly on timescales of electron acceleration and propagation. Photon shot noise in X-ray detectors is maximally antipersistent because it exhibits no correlation across time ($h \ll 0.5$).

To compute the multifractal spectra, we employ a technique known as multifractal detrended fluctuation analysis (MFDFA; J. W. Kantelhardt et al. (2002)). Prior solar flare studies have employed a wavelet-based technique (e.g. R. T. J. McAtter et al. (2007); R. T. J. McAtter & D. S. Bloomfield (2013)) to quantify the multifractal spectra, but the MFDFA technique has been shown to be faster and more robust in practice (P. Oświęcimka et al. 2006). Additionally, MFDFA has solar physics heritage, as it was applied to analyze the fractal properties of solar wind turbulence (L. F. Gomes et al. 2023).

Here, we briefly describe the steps to perform the MFDFA technique. A less general form of MFDFA is known as detrended fluctuation analysis (DFA), which is used to quantify the Hurst exponent $H = 2 - d$ —a monofractal scaling exponent, and $1 < d < 2$ a fractal dimension (C. K. Peng et al. 1993). To perform DFA, the time series is split into N segments indexed by s of length n . The segments are fit with lines and the variance $\text{Var}(n, s)$ from the each is computed for each segment s . The

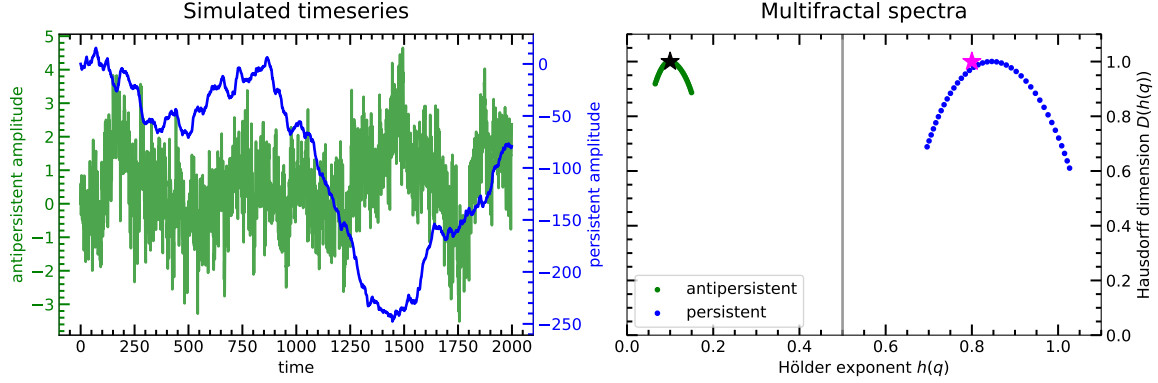


Figure 7. The MFDFA technique applied to two **simulated** time series. The time and amplitude values are in arbitrary units. The green data is “antipersistent”, akin to Poisson noise present in X-ray detectors, and is defined as fractional Brownian motion (fBm) with a Hurst exponent $H = 0.1$ (B. B. Mandelbrot & J. W. V. Ness 1968). The blue data is a “persistent” time series, which is more akin to thermal X-ray emission, defined as fBm with $H = 0.8$. The stars on the righthand plot indicate the “ground truth” time series Hurst exponents. An intuitive way to interpret the righthand plot is as a probability density of different fractal behavior across the time series. The lefthand time series are snapshots of infinite processes; in the infinite-time limit, the multifractal spectra on the right would converge to the stars. The gray line indicates the persistence/antipersistence boundary $h = 0.5$.

variance is normalized to define a fluctuation function $F(n, s) \sim \text{Var}(n, s)^{1/2}$. The fluctuation function (a measure of local complexity) depends on the length of the data segments n (a measure of scale) and scales like n^H where H is the Hurst exponent.

DFA may be generalized to the multifractal sense by exploring different moments q of the fluctuation function, i.e. $F_{\text{mf}}(n, s) \sim \text{Var}(n, s)^{1/q}$. The moment q weights short- or long-scale variations differently depending on its value, with $q = 2$ corresponding to the Hurst exponent calculation. The multifractal fluctuation function $F_{\text{mf}}(n, s)$ scales as $n^{h(q)}$ with h the Hölder exponent (J. W. Kantelhardt et al. 2002). So, from $F_{\text{mf}}(n, s)$, we may compute the multifractal spectrum. We use the open-source **fathon** Python package to evaluate the multifractal spectra (S. Bianchi 2020), which implements MFDFA as well as other fractal analysis techniques.

We apply the MFDFA technique to X-ray light curves of Flares F1 and F2 as a function of energy. Instead of plotting full multifractal spectra for each light curve, we plot only the dominant fractal behavior, which for Figure 7 would correspond to points plotted close to the magenta and black stars.

For flare F1, the behavior is plotted in Figure 8. The colored regions correspond to three different timeseries behaviors: antipersistent, persistent, and nonstationary (i.e. non-mean-reverting). The energy bands dominated by thermal emission are mainly persistent verging on nonstationary; those by nonthermal are mainly antipersistent verging on persistent; and, the thermal/nonthermal energy cross-over is characterized by a transition from persistent to antipersistent. From this summary plot, we may infer that a good choice of pseudobasis vectors for this flare would be any persistent low-energy band for the thermal pseudobasis, and any energy band which has ap-

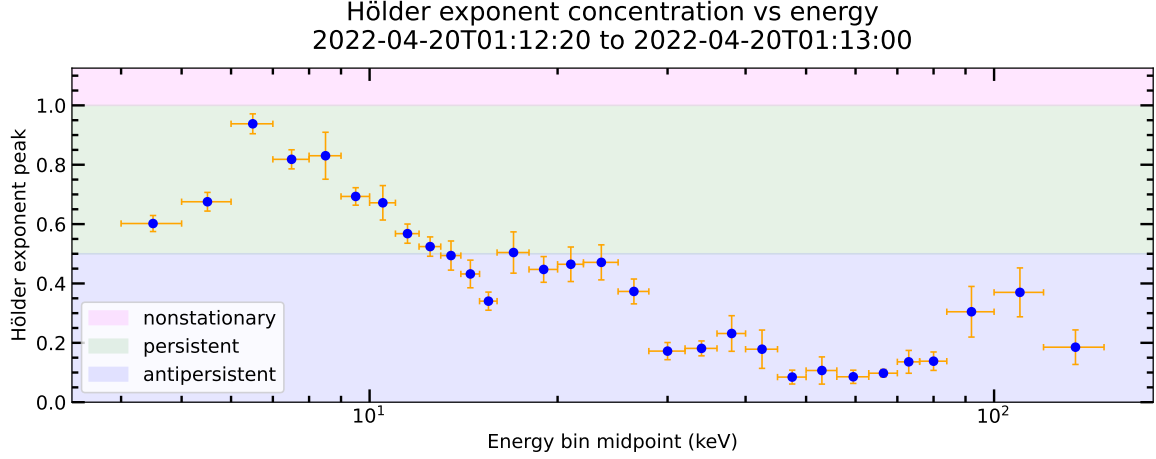


Figure 8. Multifractal spectrum peak and spread as a function of energy for Flare F1. We only focus on the most prevalent behavior of each timeseries, which corresponds to multifractal moments $q = 0$ (y value) and $q = \pm 0.2$ (y error); see (J. W. Kantelhardt et al. 2002) for information on the interpretation of the moments. The x errorbars correspond to energy bin widths. Counts data that are background-dominated (i.e. mostly Poisson noise) are very antipersistent and stay entirely in the blue region ($E \geq 28$ keV).

proximately the same dominant Hölder exponent around 20 keV for the nonthermal basis. Notably, we did not include any spectroscopic or energy information in this analysis. The fractal information is purely a function of light curve shape.

A more precise interpretation of the multifractal summary plots is, “clumps of energy bins in the fractal summary plots which all have similar Hölder exponents are likely full of counts from the same physical emission mechanism.” Figure 9 shows a similar summary plot for Flare F2, which was observed by RHESSI. Here again we see that for low energies, the time series are persistent to nonstationary. For higher energies the emission is persistent, but the Hölder exponent h error bars are larger here, in part due to the coarser time binning (fewer data points). Again we see a transition region around 20 keV which nicely correlates with the thermal/nonthermal transition region inferred from spectroscopy. There appear to be two distinct Hölder exponent clumpings at low vs. high nonthermal energies: one from 25-50 keV, and one from 50-100 keV. Perhaps these clumps correspond to two different electron populations. Again we may choose our nonthermal pseudobases based on these summary plots.

Interestingly, no statistically significant periodic pulsations were identified in either flare during the spectroscopy intervals. Quasi-periodic pulsations were investigated using the AFINO package (A. R. Inglis et al. 2015, 2016). A sympathetic flare was observed after Flare F1 at around 01:40 UTC, and this flare did exhibit significant oscillations with period ~ 27 s. Therefore, periodic behavior is not required to apply this decomposition technique, and is not necessary to make use of the multifractal spectra.

The dominant fractal behavior of X-ray light curves may be used to select and justify the choice of time pseudobases, and give an early indication of whether or not

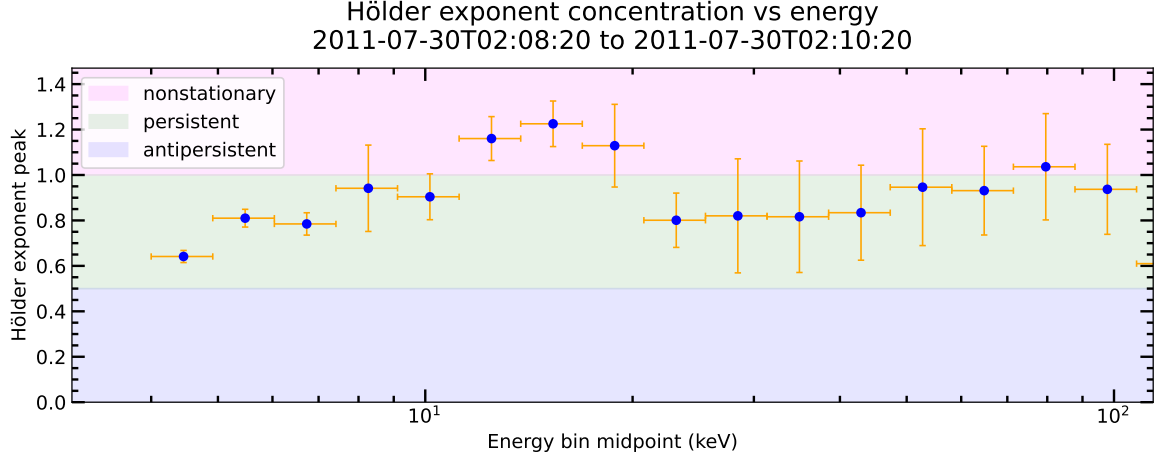


Figure 9. Multifractal summary for Flare F2, produced in the same manner as Figure 8. We see similar behavior as in the case of the STIX flare, but the nonthermal emission remains persistent even at higher energies, and the y error bars are larger. This is because there are fewer time bins across a similar analysis interval, and the higher energies are not dominated by shot noise from a radioactive calibration source.

the method will work well. These techniques may be applied to any spectrogram-like data, whether it be X-ray, radio, particle, or otherwise. You don’t need to use the multifractal formalism to get started with the temporal decomposition technique, but it is a robust way to check if you have picked good pseudobases.

6. CONCLUSION

We have developed and demonstrated a new technique for performing spectroscopy on solar flare X-ray data. Here are three main takeaways from this work:

1. Timing information can be used to aid in spectroscopy, lifting energy degeneracies which typically lead to large uncertainties, as it permits fitting thermal/nonthermal spectra independently.
2. Time-informed spectroscopy yields (sometimes orders of magnitude) more precise results than traditional spectroscopy, which impacts calculations such as the total energy contained in flare electrons.
3. The multifractal formalism gives a robust definition of “time series shape,” and may be used to select and/or verify pseudobasis light curves.

In future work, we plan to apply this technique to other wavelengths and data products, such as ground- and space-based radio observations, and space-based particle observations. We encourage readers to apply this technique to other subfields of physics, and entirely different domains.

ACKNOWLEDGEMENTS

We would like to acknowledge help from James T. McAteer with debugging an earlier version of the multifractal formalism code, and for offering his own implementation of

the wavelet transform modulus maxima method. We thank Andy Inglis for his help searching for quasiperiodic pulsations in our selected flares, and we thank him and Trevor Knuth for conversations pertaining to this work.

We acknowledge NSF CAREER grant AGS 1752268 and NASA grant 80NSSC20K1318 for funding this work.

REFERENCES

- Alaoui, M., Krucker, S., & Saint-Hilaire, P. 2019, *SoPh*, 294, 105, doi: [10.1007/s11207-019-1495-6](https://doi.org/10.1007/s11207-019-1495-6)
- Bale, S. D., Goetz, K., Harvey, P. R., et al. 2016, *SSRv*, 204, 49, doi: [10.1007/s11214-016-0244-5](https://doi.org/10.1007/s11214-016-0244-5)
- Bianchi, S. 2020, *Journal of Open Source Software*, 5, 1828, doi: [10.21105/joss.01828](https://doi.org/10.21105/joss.01828)
- Brown, J. C. 1971, *SoPh*, 18, 489, doi: [10.1007/BF00149070](https://doi.org/10.1007/BF00149070)
- Butterworth, S., et al. 1930, *Wireless Engineer*, 7, 536
- Caspi, A., Krucker, S., & Lin, R. P. 2014, *ApJ*, 781, 43, doi: [10.1088/0004-637X/781/1/43](https://doi.org/10.1088/0004-637X/781/1/43)
- Chen, B., Battaglia, M., Krucker, S., Reeves, K. K., & Glesener, L. 2021, *ApJL*, 908, L55, doi: [10.3847/2041-8213/abe471](https://doi.org/10.3847/2041-8213/abe471)
- Cheng, J., Qiu, J., Ding, M., & Wang, H. 2013, in *AAS/Solar Physics Division Meeting*, Vol. 44, AAS/Solar Physics Division Abstracts #44, 402.05
- Correia, J. P. 2024, *Scientific Reports*, 14, 10687, doi: [10.1038/s41598-024-60722-2](https://doi.org/10.1038/s41598-024-60722-2)
- Drożdż, S., Kowalski, R., Oświęcimka, P., Rak, R., & Gębarowski, R. 2018, *arXiv e-prints*, arXiv:1809.06728, doi: [10.48550/arXiv.1809.06728](https://doi.org/10.48550/arXiv.1809.06728)
- Emslie, A. G. 2003, *ApJL*, 595, L119, doi: [10.1086/378168](https://doi.org/10.1086/378168)
- Feder, J. 2013, *Fractals* (Springer Science & Business Media)
- Foreman-Mackey, D. 2016, *The Journal of Open Source Software*, 1, 24, doi: [10.21105/joss.00024](https://doi.org/10.21105/joss.00024)
- Foreman-Mackey, D., Hogg, D. W., Lang, D., & Goodman, J. 2013, *Publications of the Astronomical Society of the Pacific*, 125, 306, doi: [10.1086/670067](https://doi.org/10.1086/670067)
- Gomes, L. F., Gomes, T. F. P., Rempel, E. L., & Gama, S. 2023, *MNRAS*, 519, 3623, doi: [10.1093/mnras/stac3577](https://doi.org/10.1093/mnras/stac3577)
- Grigis, P. C., & Benz, A. O. 2004, *A&A*, 426, 1093, doi: [10.1051/0004-6361:20041367](https://doi.org/10.1051/0004-6361:20041367)
- Gustafsson, F. 1996, *IEEE Transactions on Signal Processing*, 44, 988, doi: [10.1109/78.492552](https://doi.org/10.1109/78.492552)
- Hayes, L. A., Inglis, A. R., Christe, S., Dennis, B., & Gallagher, P. T. 2020, *The Astrophysical Journal*, 895, 50, doi: [10.3847/1538-4357/ab8d40](https://doi.org/10.3847/1538-4357/ab8d40)
- Holman, G. D., Aschwanden, M. J., Aurass, H., et al. 2011, *SSRv*, 159, 107, doi: [10.1007/s11214-010-9680-9](https://doi.org/10.1007/s11214-010-9680-9)
- Inglis, A. R., Ireland, J., Dennis, B. R., Hayes, L., & Gallagher, P. 2016, *ApJ*, 833, 284, doi: [10.3847/1538-4357/833/2/284](https://doi.org/10.3847/1538-4357/833/2/284)
- Inglis, A. R., Ireland, J., & Dominique, M. 2015, *ApJ*, 798, 108, doi: [10.1088/0004-637X/798/2/108](https://doi.org/10.1088/0004-637X/798/2/108)
- Ishikawa, S.-n., Katsuragawa, M., Watanabe, S., et al. 2016, *Journal of Geophysical Research (Space Physics)*, 121, 6009, doi: [10.1002/2016JA022631](https://doi.org/10.1002/2016JA022631)
- Kantelhardt, J. W., Zschiegner, S. A., Koscielny-Bunde, E., et al. 2002, *Physica A Statistical Mechanics and its Applications*, 316, 87, doi: [10.1016/S0378-4371\(02\)01383-3](https://doi.org/10.1016/S0378-4371(02)01383-3)
- Kiplinger, A. L., Dennis, B. R., Frost, K. J., Orwig, L. E., & Emslie, A. G. 1983, *ApJL*, 265, L99, doi: [10.1086/183966](https://doi.org/10.1086/183966)
- Knuth, T., & Glesener, L. 2020, *ApJ*, 903, 63, doi: [10.3847/1538-4357/abb779](https://doi.org/10.3847/1538-4357/abb779)

- Kontar, E. P., Jeffrey, N. L. S., Emslie, A. G., & Bian, N. H. 2015, *ApJ*, 809, 35, doi: [10.1088/0004-637X/809/1/35](https://doi.org/10.1088/0004-637X/809/1/35)
- Krucker, S., Kontar, E. P., Christe, S., & Lin, R. P. 2007, *ApJL*, 663, L109, doi: [10.1086/519373](https://doi.org/10.1086/519373)
- Krucker, S., Hurford, G. J., Grimm, O., et al. 2020, *A&A*, 642, A15, doi: [10.1051/0004-6361/201937362](https://doi.org/10.1051/0004-6361/201937362)
- Lin, R. P., & Hudson, H. S. 1976, *SoPh*, 50, 153, doi: [10.1007/BF00206199](https://doi.org/10.1007/BF00206199)
- Lin, R. P., Dennis, B. R., Hurford, G. J., et al. 2002, *SoPh*, 210, 3, doi: [10.1023/A:1022428818870](https://doi.org/10.1023/A:1022428818870)
- Mandelbrot, B. B., & Ness, J. W. V. 1968, *SIAM Review*, 10, 422. <http://www.jstor.org/stable/2027184>
- McAteer, R. T. J., & Bloomfield, D. S. 2013, *ApJ*, 776, 66, doi: [10.1088/0004-637X/776/2/66](https://doi.org/10.1088/0004-637X/776/2/66)
- McAteer, R. T. J., Young, C. A., Ireland, J., & Gallagher, P. T. 2007, *ApJ*, 662, 691, doi: [10.1086/518086](https://doi.org/10.1086/518086)
- Oświęcimka, P., Kwapień, J., & Drożdż, S. 2006, *Phys. Rev. E*, 74, 016103, doi: [10.1103/PhysRevE.74.016103](https://doi.org/10.1103/PhysRevE.74.016103)
- Peng, C. K., Buldyrev, S. V., Goldberger, A. L., et al. 1993, *PhRvE*, 47, 3730, doi: [10.1103/PhysRevE.47.3730](https://doi.org/10.1103/PhysRevE.47.3730)
- Qiu, J., Cheng, J. X., Hurford, G. J., Xu, Y., & Wang, H. 2012, *A&A*, 547, A72, doi: [10.1051/0004-6361/201118609](https://doi.org/10.1051/0004-6361/201118609)
- Saint-Hilaire, P., & Benz, A. O. 2005, *A&A*, 435, 743, doi: [10.1051/0004-6361:20041918](https://doi.org/10.1051/0004-6361:20041918)

APPENDIX

A. DETAILS: THE MULTIFRACTAL FORMALISM

Multifractal systems can be described by a distribution of Hausdorff dimensions plotted as a function of Hölder exponent; this is the multifractal spectrum. Intuitively, the multifractal spectrum quantifies how local function sharpness (Hölder exponent) fills the space (Hausdorff dimension) of the timeseries. The multifractal spectrum can be interpreted as a probability density $p(h(q))$ of Hölder exponents. Here we define the Hölder exponent and give a pictorial representation of how Hölder exponents envelop the local behavior of time series. We then define the Hausdorff dimension for a generic metric space and relate it to the multifractal analysis.

The Hölder exponent is an example of a singularity exponent. The singularity exponent describes the local function sharpness and is defined as in [Equation A1](#), where t is the independent variable, $f(t)$ is the function under analysis, τ is some fixed time, and $p(t)$ is the time-dependent singularity exponent enveloping the function about $t = \tau$ ([R. T. J. McAtter et al. 2007](#); [J. Feder 2013](#)).

$$f(t - \tau) \sim \tau^{p(t)} \quad (\text{A1})$$

The Hölder exponent is a singularity exponent which has useful properties. First we define the set $C^\alpha(\tau)$ as in [Equation A2](#) for a polynomial P_m of degree m , $m < \lfloor \alpha \rfloor$, at some time $t = \tau$.

$$|f(t) - P_m(t - \tau)| \leq C |t - \tau|^\alpha \quad (\text{A2})$$

The timeseries $f \in C^\alpha(\tau)$ when [Equation A2](#) is satisfied; that is, when the local time series behavior scales like a power law on top of an m^{th} order polynomial. Then, the Hölder exponent $h(f, \tau)$ is defined as in equation [Equation A3](#).

$$h(f, \tau) = \sup \{ \alpha > 0 \mid f \in C^\alpha(\tau) \} \quad (\text{A3})$$

The Hölder exponent is the supremum (least upper bound) α that describes the local scaling of the timeseries $f(t \approx \tau)$ ([R. T. J. McAtter et al. 2007](#)). **Because the local scaling is a power law, smaller $h(\tau)$ describe sharper features than larger $h(\tau)$ as illustrated in [Figure 10](#).** For fractal time series, it is usually the case that $0 < \alpha < 1$, but not always.

The other dimension in the multifractal spectrum is on its y axis, the Hausdorff dimension. Informally, the Hausdorff dimension describes how much space a measurable object fills. In the multifractal context, it can be interpreted as a probability distribution of Hölder exponents.

We may define the Hausdorff dimension on any metric space, in particular that of Hölder exponents on a time series. Let X be a metric space—a set of points with a metric function; for example, the set of real numbers \mathbb{R} is a metric space

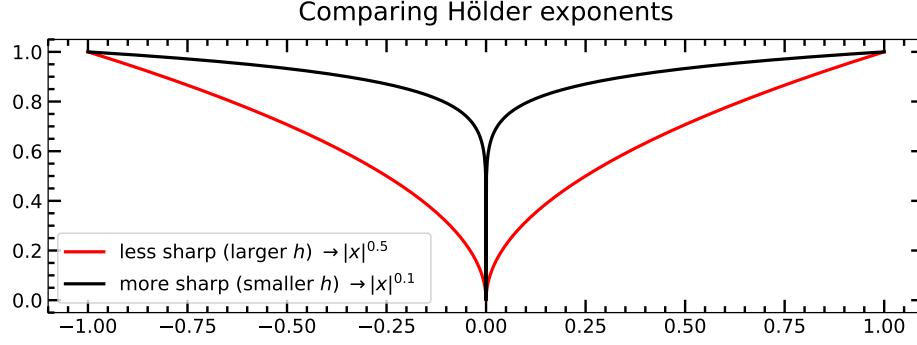


Figure 10. Comparison of local Hölder exponent envelopes about $x = 0$. Sharper features are described by smaller exponents.

with $x, y \in \mathbb{R}$ and metric function $g(x, y) = |x - y|$. Let $S \subset X$ and the diameter $\text{diam}(S) = \sup\{g(x, y) \mid x, y \in S\}$.

Define the incomplete Hausdorff measure for the set S as in Equation A4. I is some (potentially infinite) indexing set, U_i is a simple shape which covers part of the set S , δ is the maximum allowed diameter, and d is a power which weights the summation (the “moment” of the sum). The equation sums up the d^{th} powers of the diameters of simple shapes—balls, boxes, or otherwise—covering the metric space S . The maximum diameter δ may be made arbitrarily small.

$$H_\delta^d(S) = \inf \left\{ \sum_{i \in I} (\text{diam}(U_i))^d : \bigcup_{i \in I} U_i \supseteq S, \text{diam}(U_i) < \delta \right\} \quad (\text{A4})$$

Now define the (complete) Hausdorff measure as in Equation A5.

$$\begin{aligned} H^d(S) &= \sup_{\delta > 0} H_\delta^d(S) \\ &= \min_{\delta > 0} H_\delta^d(S) \\ &\equiv \lim_{\delta \rightarrow 0} H_\delta^d(S) \end{aligned} \quad (\text{A5})$$

The Hausdorff measure is $H^d(S)$. There exists some “transitional” d for which the Hausdorff measure goes from $H^d(S) = \infty$ to $H^d(S) = 0$ which may be found by evaluating the limit $\delta \rightarrow 0$.

From the Hausdorff measure define the Hausdorff dimension, $D(S)$ as in Equation A6.

$$D(S) = \inf \{d \geq 0 : H^d(S) = 0\} \quad (\text{A6})$$

In the MFDFA case we approximate the Hausdorff dimension as $D(h(q))$ as in S. Bianchi (2020), where the metric function on the set $h(q)$ is some distance between Hölder exponents dependent upon the local function sharpnesses and fluctuation function $F_{\text{mf}}(n, s)$ as described in section 5. J. W. Kantelhardt et al. (2002), section 2.2, describes the mathematical equivalence of the fluctuation function to the way folks traditionally compute the multifractal spectrum, which is via the so-called

box-counting method. There, the balls U_i are replaced by boxes and a statistical mechanics approach is applied to define the fractal scaling (the $p(t)$ from [Equation A1](#)) as a function of the number of boxes it takes to cover parts of the time series at different box sizes.

B. CORNER PLOTS: TRADITIONAL VS. DECOMPOSED SPECTROSCOPY

Corner plots offer a fast way to visualize parameter covariances and marginal posterior distributions. All corner plots produced in this work were made using `corner.py` ([D. Foreman-Mackey 2016](#)).

95% posterior intervals are annotated on all of the marginal distributions in the corner plots as dashed lines. The titles have the (2.5%, 50%, 97.5%) quantiles annotated in $P_{-\delta P_2}^{+\delta P_1}$ fashion, with P a parameter value and δP_i the one-sided uncertainty. The values annotated are the same as the 95% intervals given in the text, just written in a different way. The median values of the posteriors are annotated in the titles in order to be more congruous with the histograms. The best-fit values are annotated as the red crosses in each plot.

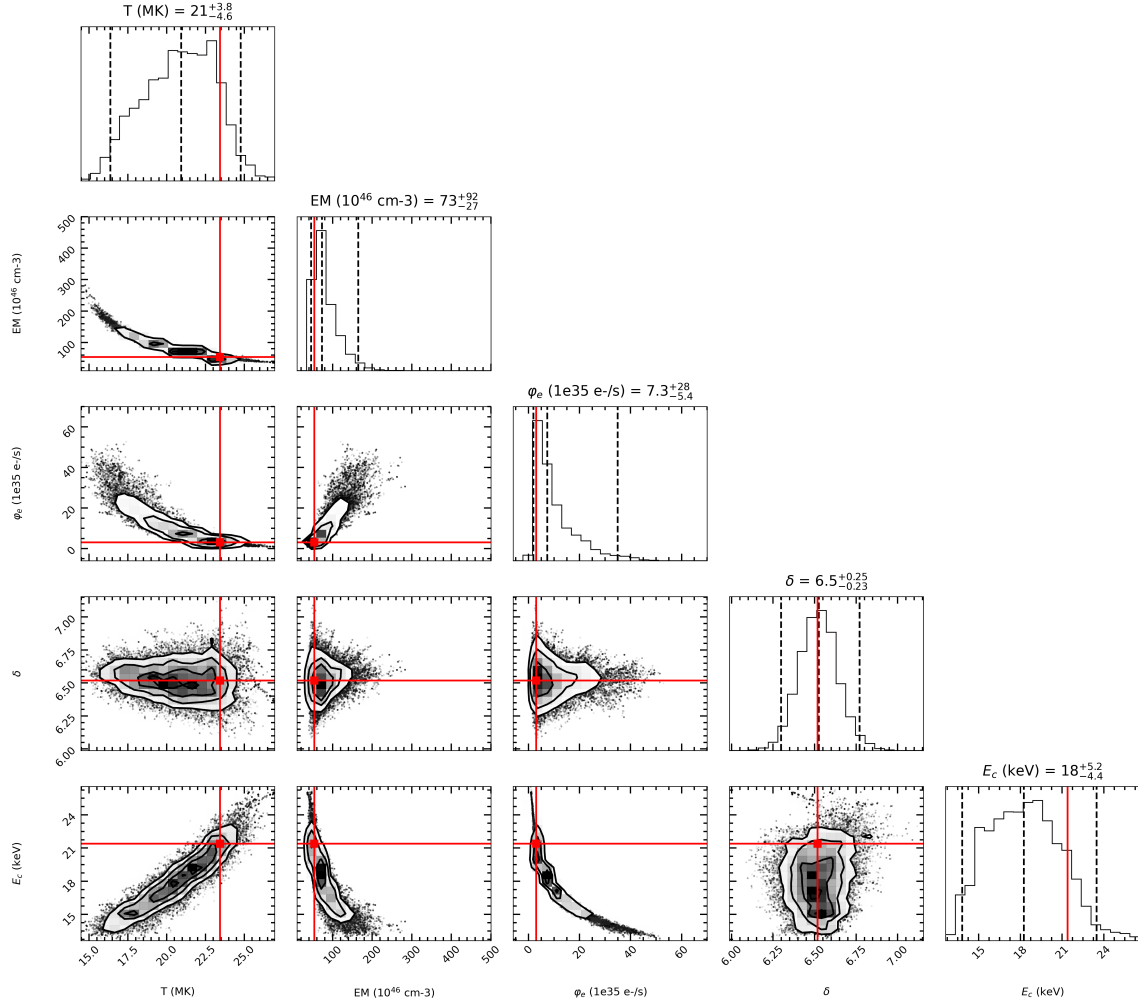


Figure 11. Corner plots for parameters fit using traditional spectroscopy on Flare F1 across its analysis interval. The red crosshairs mark the best fit parameters found via Levenberg-Marquadt minimization.

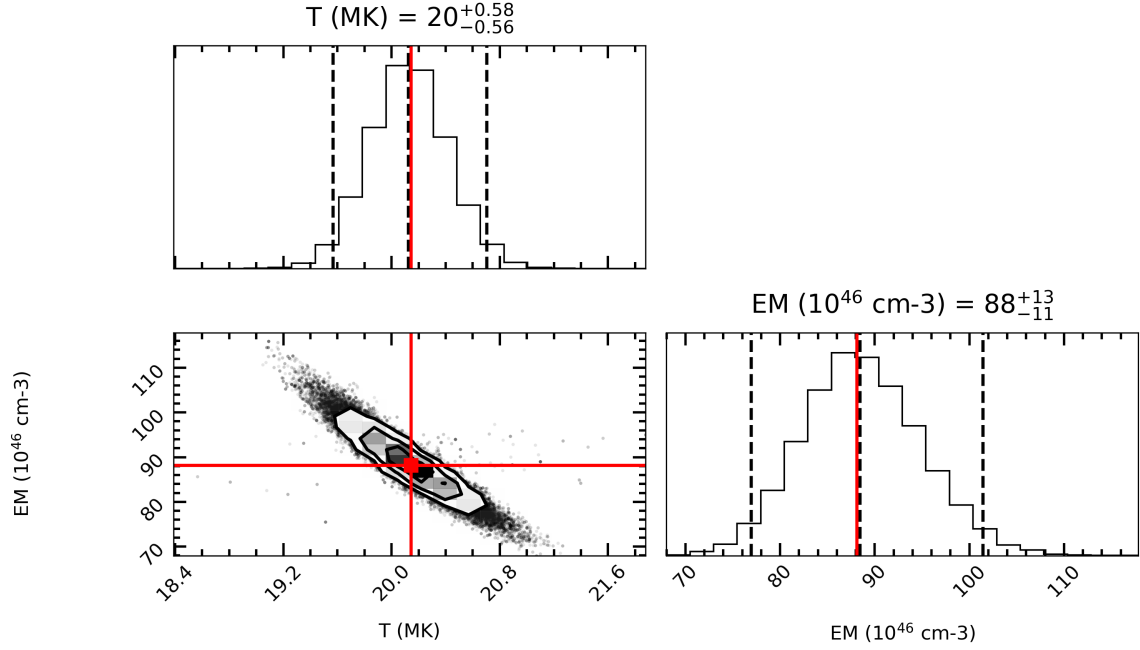


Figure 12. Corner plots for thermal parameters fit using time-decomposed spectroscopy on Flare F1 across its analysis interval. The red crosshairs mark the best fit parameters found via Levenberg-Marquadt minimization.

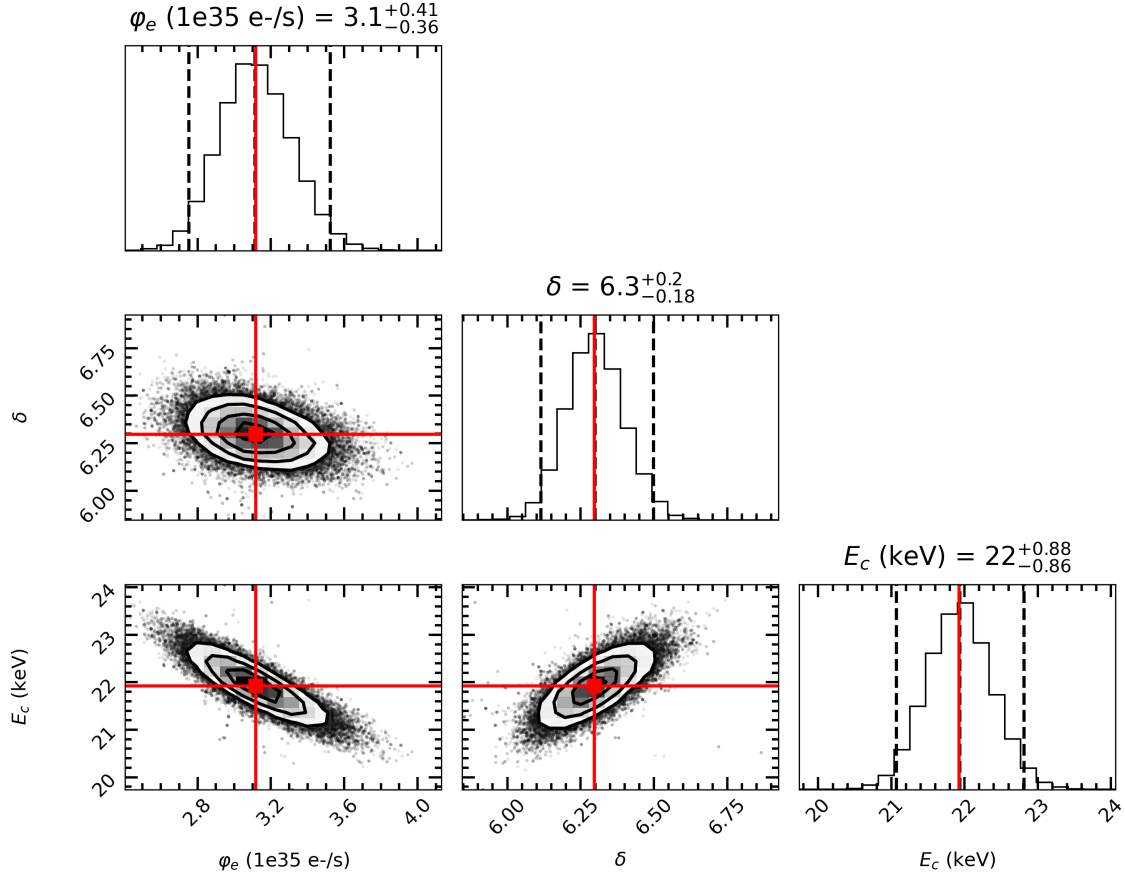


Figure 13. Corner plots for nonthermal parameters fit using time-decomposed spectroscopy on Flare F1 across its analysis interval. The red crosshairs mark the best fit parameters found via Levenberg-Marquadt minimization.

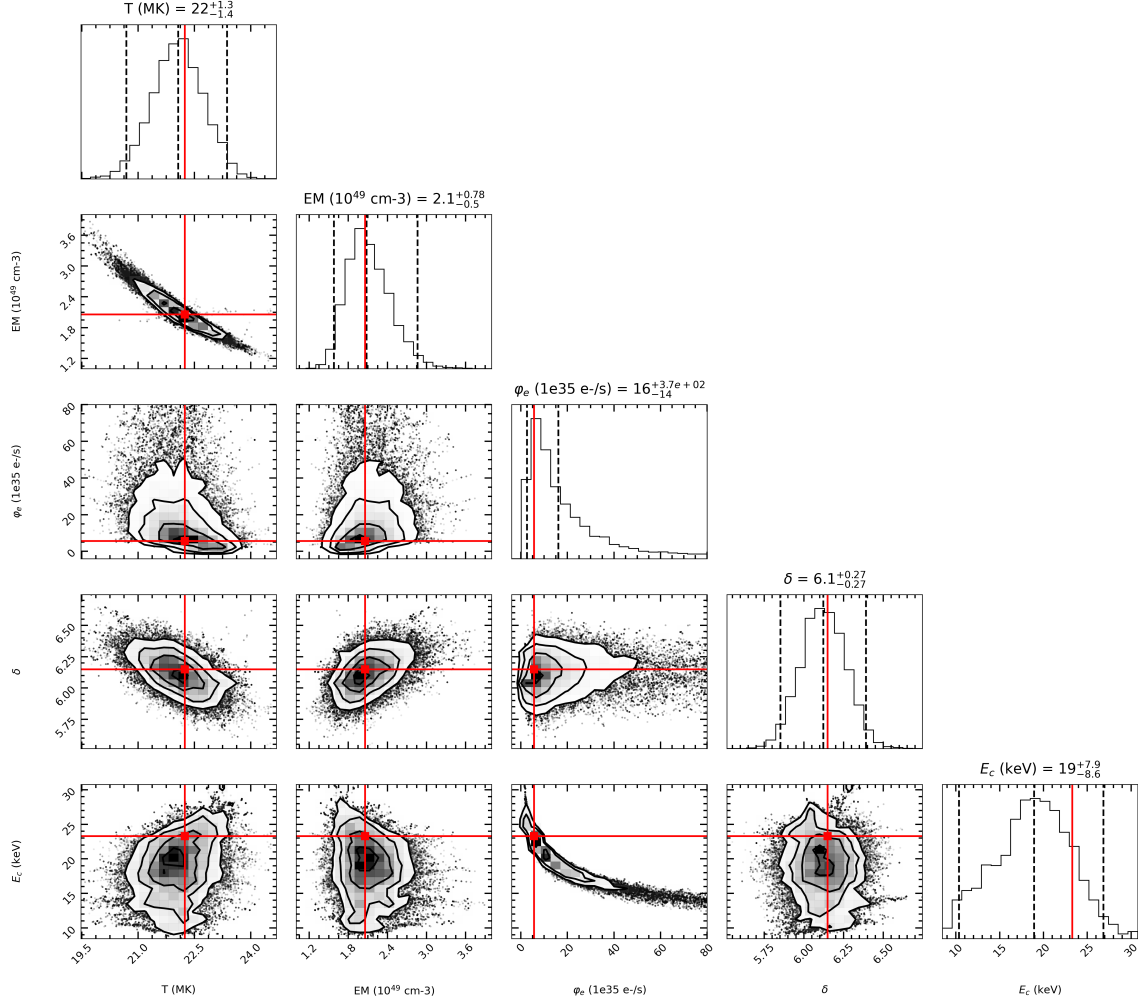


Figure 14. Corner plots for parameters fit using traditional spectroscopy on Flare F2 across its analysis interval. The red crosshairs mark the best fit parameters found via Levenberg-Marquadt minimization.

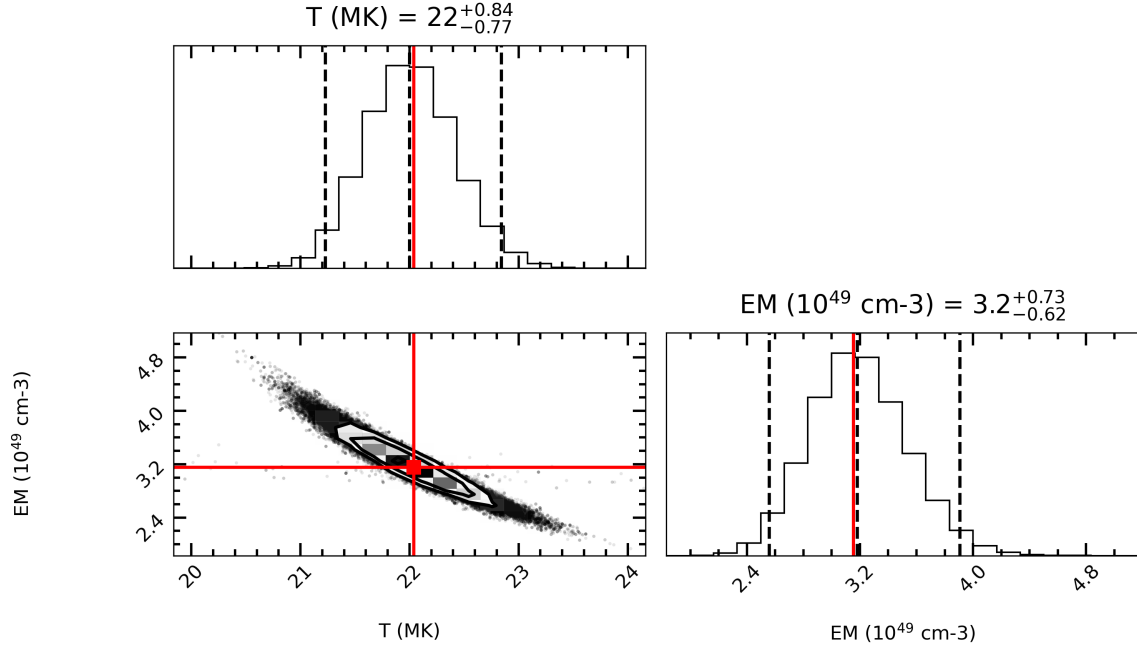


Figure 15. Corner plots for thermal parameters fit using time-decomposed spectroscopy on Flare F2 across its analysis interval. The red crosshairs mark the best fit parameters found via Levenberg-Marquadt minimization.

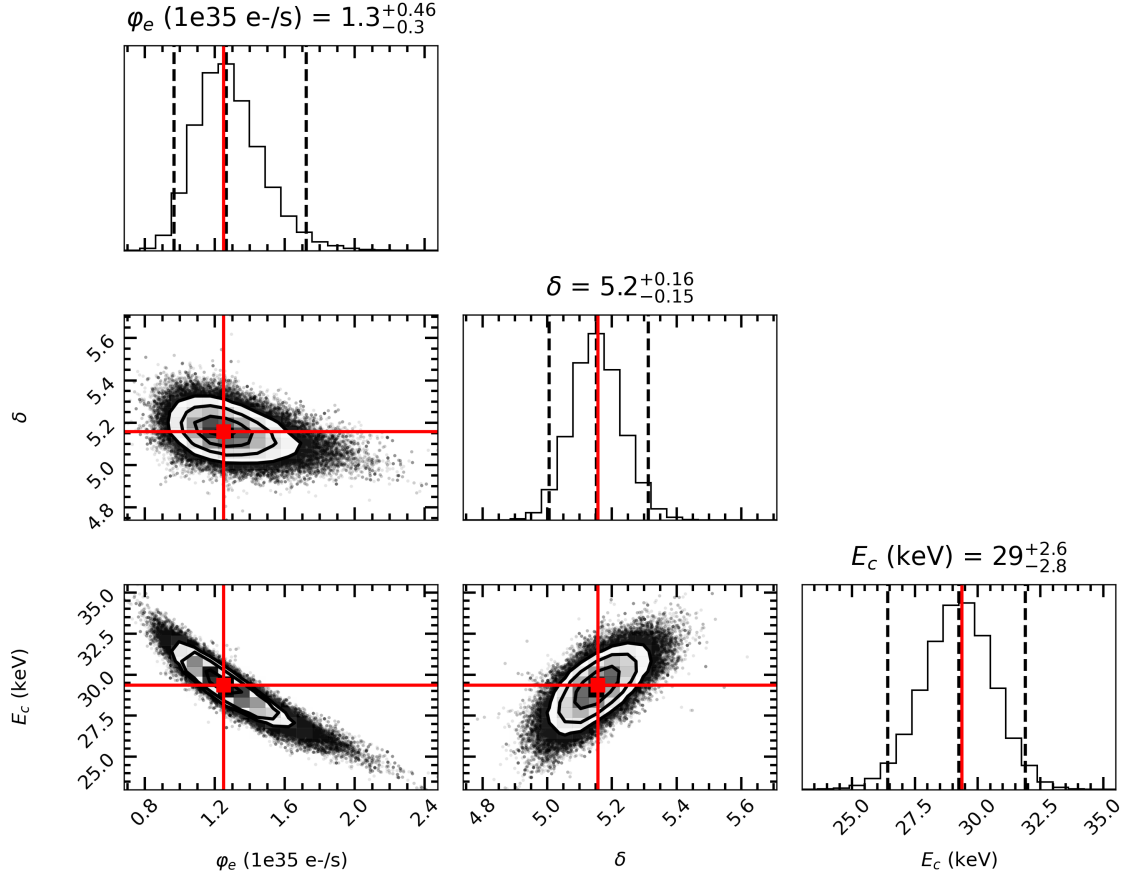


Figure 16. Corner plots for nonthermal parameters fit using time-decomposed spectroscopy on Flare F2 across its analysis interval. The red crosshairs mark the best fit parameters found via Levenberg-Marquadt minimization.